

Mapping and Assessing Spatial Extent of Floods from Multitemporal Synthetic Aperture Radar Images: A Case Study over Chennai City, India

Sreechanth Sundaram

Vellore Institute of Technology: VIT University

Suresh Devaraj

Saveetha Engineering College

Kiran Yarrakula (✉ kiran@gkciet.ac.in)

Ghani Khan Chaudhury Institute of Engineering and Technology

Research Article

Keywords: Flood, SAR, Sentinel-1A, Urban Floods, Remote Sensing

Posted Date: May 19th, 2022

DOI: <https://doi.org/10.21203/rs.3.rs-1565050/v1>

License:  This work is licensed under a Creative Commons Attribution 4.0 International License.

[Read Full License](#)

Version of Record: A version of this preprint was published at Environmental Science and Pollution Research on March 23rd, 2023. See the published version at <https://doi.org/10.1007/s11356-023-26467-7>.

Abstract

Urban floods are more concerned in recent days due to their substantial effect in loss of human lives and properties. Due to climate change, urban floods are frequently observed in many parts of the world. Flood events in Chennai city is a frequent scenario due to rapid increase in the density of population. Adyar river watershed and surrounding urban cover is focused in the present study. The present study aims at mapping flooded region using Sentinel 1 datasets over Chennai city. Series of Sentinel-1A image is collected before, during and after floods for mapping the extent of flood and mapping risk zones in Adyar watershed. Methodologies such as ISODATA Technique, Multi-Temporal Analysis, Thresholding Method, PCA and ICA Analysis and Grey Level Co-Occurrence Matrix are adopted for the extraction of flooded extent from the SAR datasets. Analysis performed over the Chennai city provided promising results in the extraction of flooded extent with Thresholding Method and Grey Level Co-Occurrence Matrix being the dominant of all the methods. Though higher accuracy is obtained in the extraction of flooded extent, limitation of layover, foreshortening and shadow is experienced in the built up region for the extraction of flooded pixels.

1. Introduction

Floods are identified to be one of the frequent natural disaster recorded across the globe (Chaudhary and Piracha 2021). Floods are differentiated by their location of occurrences, such as riverine floods, coastal floods, flash flood and urban floods (Sundaram et al. 2021). Among the different types of floods, urban floods are proved to be the most devastating, as they affect the livelihood of the highly dense populated location leading to loss of human life and economy of the country (Dube et al. 2021). Rapid development of urban areas and settlements towards cities, is one the major reason for exposure of people and properties flood risk (Ilam Vazhuthi and Kumar 2020). Being the second largest populated country in the world, India has a dense population with around 33.3% of the people residing in urban locations (Ehrlich et al. 2021). Increase in urbanisation leads results in over exploitation of the existing resources due to the increase in demand (Kookana et al. 2020). Over the past decade, urbanisation has led to a drastic change in the land cover features resulting in climate change, which affects the natural environment (Kookana et al. 2020). Flood occurrence over the past decade has increased in major cities such as Mumbai, Chennai, Delhi, Hyderabad, etc. and it is suggested that the exploitation of resources and improper planning is the major reason for flood occurrences (Surampudi and Yarrakula 2020). Remote sensing and GIS is identified to be the optimal tool for mapping the extent of water bodies and estimating the flooded extent (Ouled Sghaier et al. 2018). Adopting the space technologies can help in disaster mitigation and management purposes and also in establishing a well-defined drainage network and routing (Das et al. 2007).

Space platforms are widely adopted to acquire information of the earth surface using various technologies at higher spatial and temporal resolution (Fu et al. 2020). Since the launch of first satellite in the year 1957, several space missions with multi-spectral, hyperspectral and microwave remote sensing systems are utilised for wide range of applications (Tatem et al. 2008). Mapping and monitoring of

various hazards like floods, earthquakes, volcanic activity, wildfires, landslide and glacier movements are effectively carried out using remote sensing and GIS techniques (Devaraj and Yarrakula 2020b, a). Organisations including United States Geological Survey (USGS), National Aeronautics Space Administration (NASA), European Space Agency (ESA), Indian Space Research Organisation (ISRO), Japan Aerospace Exploration Agency (JAXA) and Canadian Space Agency (CSA) are some of the recognised space agencies around the world that have launched several missions for acquiring information about the earth (Ustin and Middleton 2021). Various space missions have been launched since the 1950s and the evolution of satellites is shown in Fig. 1.

Figure 1. Evolution of space age with few major space missions since the 1950s.

Application of space mission includes astronomical, communication, earth observation, navigation, reconnaissance and weather applications, whereas sensor types include active sensors (Lidar, Radar and Scatterometer) and passive sensors (spectrometer, spectroradiometer and hyperspectral radiometer) (Cooper and Smith 2019). Few widely adopted passive and active sensors used in satellite platforms are listed in Table 1.

Table 1
Passive and Active Space Missions

S.No	Satellite - Platform	Type
1	Global Precipitation Measurement	Radar (Active Sensor)
2	Sentinel-1A, Sentinel-1B, 3A	Radar (Active Sensor)
3	Tropical Rainfall Measuring Mission (TRMM)	Imager (Passive Sensor)
4	Landsat TM, ETM+, OLI	Radiometer (Passive Sensor)
5	NASA-ISRO SAR Mission (NISAR)	Radar (Active Sensor)
6	Advanced Land Observing Satellite (ALOS)	Radiometer (Passive Sensor)
7	Hyperion EO-1	Imaging Spectrometer (Passive Sensor)
8	European Remote Sensing satellite (ERS-2)	Microwave (Active Sensor)

1.1 Detection of Open Water Using Optical Sensors

Optical sensors are passive sensors used to obtain multispectral imagery using the visible portion of the electromagnetic spectrum (Xue and Su 2017). Each multispectral imagery consists of 3 to 11 bands containing information about the earth surface features (Suresh et al. 2018; Reddy et al. 2019).

Numerous algorithms were developed for extracting the water from multispectral imagery. Normalized Difference Water Index (NDWI), Modified Normalized Difference Water Index (MNDWI), Water Index (WI), Automatic Water Extraction Index (AWEI), Tasseled Cap Wetness Index (TCW), Land Surface Water Index (LSWI) are some of the widely adopted indices for the extraction of surface water features (Rad et al.

2021). Algorithms such as Support Vector Machine (SVM), Iterative Self-Organizing Data Analysis Technique (ISODATA), K-means, Decision tree based supervised and unsupervised classification methods are used for demarcating the water extent precisely (Jiang et al. 2021). Landsat series, Spot series, Worldview series, Hyperion, Moderate Resolution Imaging Spectroradiometer (MODIS), Advanced Spaceborne Thermal Emission and Reflection (ASTER), GeoEye series, Indian Remote Sensing (IRS) are some of the multispectral data imagery widely used (Beiranvand Pour et al. 2019). Limitations exist in adopting the optical imageries for mapping flooded extent due to its inability to penetrate through clouds during rainfall (Suresh and Yarrakula 2018).

To overcome the limitations of optical imageries, Synthetic Aperture Radar (SAR) images are introduced with the ability to penetrate through clouds (Huang et al. 2015). Among various spaceborne and aerial sensors available, Synthetic Aperture Radar (SAR) is the most reliable way for mapping and monitoring the extension of water bodies during floods (Vickers et al. 2019). The capability of day and night functionality and gathering data during all weather conditions makes SAR systems more reliable than passive sensor systems (Misra 2017). SAR system also able to penetrate through the canopy at certain frequencies and polarization (Manavalan 2018). Temporal resolution of SAR systems is comparatively less than passive sensors systems and provides high resolution observations of flood inundated regions (Devrani et al. 2022). Each SAR system operate at a particular frequency, collecting both amplitude and phase information (Pepe and Calò 2017). Increase in spatial resolution and accuracy of SAR images, decreases the coverage area based on acquisition mode (Ling et al. 2021). Frequency and wavelength of the SAR systems plays a dominant role in deciding the interaction of surface features with the incident signals from the radar platform (Martinis and Rieke 2015). Every band operating at different frequency and wavelength are used for different applications (Bousquet 2017). The frequency and wavelength in SAR systems are inversely related to each other (G Palm et al. 2020). Table 2 shows various SAR bands, their frequency and wavelength.

Table 2
Various Radar Bands, Frequency and Wavelength

Band	Frequency (GHz)	Wavelength (cm)
P	0.255–0.390	133 – 76.9
L	0.390–1.550	76.9–19.3
S	1.550–4.20	19.3–7.1
C	4.20–5.75	7.1–5.2
X	5.75–10.90	5.2–2.7
K	10.90–36.0	2.7–0.83
Ku	10.90–22.0	2.7–1.36
Ka	22.0–36.0	1.36–0.83
Q	36.0–46.0	0.83–0.65
V	46.0–56.0	0.65–0.53
W	56.0–100	0.53–0.30

Development of SAR sensors for detection of floods can aid in accurate mapping of flooded regions by adopting suitable processing methods and techniques (Zhang et al. 2020). Reduction of noise by speckle removal and by means of filtering helps in mapping floods more effectively (Choi and Jeong 2019). SAR datasets are basically greyscale imageries holding amplitude and phase information, which can be used for accurate delineation of floods by acquiring high resolution data and interpretation of information through backscatter analysis (Zhang et al. 2020). Lower the backscatter values represents smooth surfaces such as water bodies and roads, with the backscatter values below – 20 Db (Nagai et al. 2021). Moderate backscatter results represents moderate vegetation or agricultural crops, higher backscatter values represents dense vegetation such as forests and very high backscatter values represents settlements or man-made objects (Harfenmeister et al. 2019). Recent radar sensors aboard of RADARSAT – 2 (C-Band), TerraSAR -X (X-band) and COSMO - SkyMed (X-band) offers data at finer resolution up to 3m. Sentinel mission of European Space Agency (ESA) offers SAR data openly available for different end user and scientific community (Chatenoux et al. 2021).

Sentinel mission was launched by European Space Agency (ESA) in the year 2014, which made the availability of Sentinel SAR mission data to end users. Sentinel-1 mission consists of two polar orbiting satellites, such as 1A and 1B, both providing SAR data imaging all global landmass (Nagler et al. 2015). Sentinel 1A data revisit duration is about 12 days and has a pixel spacing about 10m. Both Sentinel-1A and Sentinel-1B operates in C band frequency (5.405GHz). In the present study, Sentinel 1 Ground Range Detected (GRD) data of VV polarization is utilised for the extraction of the water bodies (Soudani et al. 2021).

2. Study Area

Capital city of the Tamil Nadu state, Chennai is referred as the Gateway to South India with along costal line of about 43 km. Covering an area of about 178.20 sq.km, three rivers namely Cooum, Adyar and Kosasthalaiyar flows through the Chennai city. All the three rivers are connected by the Buckingham canal that links four reservoir tanks such as Red Hills, Cholavaram, Poondi and Chembarambakkam along with 16 minor waterways. The present study is focused on analysing the impact of floods along the Adyar watershed that lies between 80°11'9.106"E and 80°15'54.819"E longitude and 13°1'8.513"N and 13°3'29.645"N latitude covering an area of 330 sq.km. Chennai city experiences 40°C temperature during summer and receives an rainfall average rainfall of 400 mm and 700 mm from North-East and South-West monsoon respectively. Geographical location of the study area is shown in Fig. 2 and the details of Adyar River are shown in Table 3.

Table 3
Adyar River Profile

River	Adyar
Origin	Adanur Tank Near Guduvancherry
Location Of Confluence With Bay Of Bengal	Adyar Mouth
Total Length In km	42.5
Length In City Limits In km	15
Length In CMA In km	25
Bed Width In meter	10.50 To 200
Anticipated Flood Discharge/Capacity In cusecs	60000/39000
Flood Discharge In 2005 In cusecs	55000
Flood Discharge From Chembarambakkam In 2015 In cusecs	29000
(Source: Chennai Metro Water Supply and Sewage Board, CMWSSB)	

Since 1976, the banks of Adayar river has affected by floods. In 2015, due to el-nino effect, Chennai city received highest rainfall of about 1612.10 mm leading to a devastating floods. During the flood event, Guindy, Adyar, Velacherry, T-Nagar, Ashok Nagar, Tambaram, Guduvancherry and Chennai International Airport are some of major areas affected by floods. Excessive precipitation was identified to be the major factor that triggered floods in Chennai. Extreme rainfall was recorded on November 8th -9th, November 16th -17th and 30th November – 1st December, leading to the disaster event. Figure 3 shows the rainfall observed in chembarambakkam reservoir gauge station of Adayar River Watershed and Fig. 4 represents the storm water outflow from different locations in Chennai city.

3. Methodology

Boundary of the Adyar watershed is extracted from SRTM DEM by using Arc-hydro tools and Land Use Land Cover (LULC) maps for the year 2005, 2010 and 2015 are prepared by using Landsat imageries for quantifying the changes in the watershed over years. NDWI (Normalised Difference Water Index) is calculated using the bands of Landsat datasets for the retrieval of the water bodies in the region. Several classification methods such as Multi-temporal mapping, Change detection analysis, Textural analysis, Principal Component Analysis (PCA), and Independent Component Analysis (ICA) are used for the extraction of waterbodies from SAR datasets to evaluate the flooded extents. The detailed methodology adopted in the present study is shown in Fig. 5. Tables 4 and 5 lists the data specification of Sentinel-1 and landsat datasets utilised in the present study.

Table 4
Sentinel-1A Data Specifications

S.No	Sensor	Swath	Band	Pixel spacing	Polarisation	Date of Acquisition
1	Sentinel-1A	IW	C- Band	10x10 m	VH + VV	2015-11-12
						2015-11-24
						2015-12-06
						2015-12-18

Table 5
Landsat Mission Data Specification

S.No	Satellite	Bands	Resolution (m)	Scene Size (km)	Revisit (days)
1	Landsat TM	7	30	170*183	16
2	Landsat 8 OLI	11	30	170*183	16

4. Results And Discussion

Remote sensing products are exposed to different types of noise and distortions (Rasti et al. 2018). Several levels of processing such as radiometric calibration, atmospheric correction and geometric correction are carried out considering the sensor characteristics, atmospheric contents and weather for the correction of satellite images to reduce noise and increase the accuracy of information extracted from data (Prieto-Amparan et al. 2018). Although the pre-processing steps of Landsat data products and sentinel data are similar, the process results differs because of change in sensor, data type and data interpretation (Song et al. 2021).

Land use and land cover (LULC) map helps in prediction of development and deterioration of features classes such as vegetation, urban, forest, waterbodies, etc (Wang et al. 2021). LULC accuracy is limited to resolution of the satellite image and factors such as snow cover, cloud cover, data availability, sun angle and seasonal changes (Talukdar et al. 2020). LULC have wide range of applications such as multi-temporal mapping, allowing users to analyse the variation in land cover pattern over a particular region

(Vivekananda et al. 2021). LULC map for Adyar watershed for the years 2005, 2010 and 2015 are generated with the combination of supervised and unsupervised classification and is shown in Fig. 6. Percentage of various land use and land cover classes between the years are shown in Table 6 with a classification accuracy of 83%, 82% and 86% for the years 2005, 2010 and 2015 respectively. Figure 7 represents the variation of each LULC features in Adyar watershed over years.

Table 6
Percentage of Features in Adyar River Basin

Year	Water (%)	Built-Up (%)	Vegetation (%)	Bareland (%)	Total (%)
2005	13.820671	19.293946	36.46737	30.417967	100.00
2010	15.479294	25.116587	34.193568	25.2121	100.00
2015	14.678443	35.360468	29.455729	20.50651	100.00

Sentinel-1A SAR data is used in the study for extracting the flooded region of Chennai city. Classification method, Texture analysis, Multi-Temporal analysis, Change detection analysis and Thresholding method are used in the study for the extraction flooded regions from SAR image.

4.1 Unsupervised Classification Using ISODATA Technique

ISODATA (Iterative Self-Organizing Data Analysis Technique), a novel method of data analysis and pattern classification based on the spectral signature (Ruggeri et al. 2021). In SAR data such as Sentinel-1A, classification is restricted due to several factors, such as absence of spectral capability and black and white composite of processed SAR data (De Luca et al. 2021). In such cases, identification of ground objects is challenging and unsupervised methods are adopted for identifying the surface feature classes. ISODATA Classification of SAR images for Adyar watershed is carried out and the backscatter values are calculated and range of water presence is identified. Water bodies extent extracted from the sentinel 1 datasets during the flooded event are shown in Fig. 8.

4.2 Multi-Temporal Analysis and RGB Generation

Multi temporal mapping is basically a system of producing colour difference images based upon the temporal changes in a particular location (You et al. 2020). The process includes pre-processing of SAR images and summing up the black and white radar images into RGB. The degree of change is represented by the intensity colour change. Multi temporal image analysis requires multiple datasets of different time periods, usually pre flood, during and post flood data for multi temporal mapping of inundated regions. Result obtained is widely adopted to segregate the flooded and non-flooded regions as shown in Fig. 9.

Figure 8. Unsupervised Classification of Sentinel 1A SAR Data (a) 12th November 2015 (b) 24th November 2015 (c) 06th December 2015 (d) 18th December 2015

4.3 Thresholding Method for extraction of floods

SAR backscatter values are used extract the flood inundated regions based on the suitable threshold values (Zhang et al. 2020). Backscatter range in which the flooded regions are identified, is detected and raster colour slicing technique is used to classify the image. The flooded region classification using threshold method is shown in Fig. 10.

4.4 PCA and ICA Analysis for Enhancing Flooded Areas

Principal Component Analysis (PCA) is used for change detection on polarimetric multi-temporal SAR data (Baronti et al. 1994). Independent Component Analysis (ICA) is a technique used to classify the image for detecting the objects with unknown spectral signatures (Dabiri and Lang 2018). The limitation ICA is the number of objects classified is based on the number of available spectral bands. PCA image analysis of a temporal image series is used to reduce temporal autocorrelation thereby increasing the suitability of the data for image segmentation and classification. ICA is used for speckle reduction and ground object classification. Figure 11 (a) shows the PCA on multi-temporal sentinel 1A SAR data and Fig. 11 (b) shows the ICA on multi-temporal sentinel 1A SAR data.

4.5 Grey Level Co-Occurrence Matrix

Grey-Level Co-occurrence Matrix (GLCM) known as grey-level spatial dependence matrix is a statistical method used for inspecting the spatial relationship between the pixels in the two dimensional grid (Vargas et al. 2011). GLCM is the measure of occurrence of different combinations of the grey levels (intensity) appear in the image (Zainal et al. 2013). Information about the spatial distribution and tonal variation can be estimated based on different textures of the features. Table 7 represents the formula used to calculate GLCM statistics in the present study.

Table 7
GLCM Statistics

Contrast CON	It is called the difference moment of GLCM and it measures the spatial frequency (Level of detail) of the image.	$\sum_{i,j=0}^{N-1} P_{i,j} (i - j)^2$
Energy ENE	It measures the textural uniformity (colour and texture) and detects the disorder in textures. Also known as uniformity or the angular second moment (ASM).	$\sum_{i,j} P(i,j)^2$
Entropy ENT	It measures the disorder or complexity of the image. Texturally uneven image results in increased entropy	$\sum_{i,j=0}^{N-1} P_{i,j} (-1 \ln P_{i,j})$
Homogeneity HOM	It is the inverse difference moment, measures the homogeneous elements (similar backscatter – grey values) of the image.	$\sum_{i,j=0}^{N-1} \frac{P_{i,j}}{1 + (i-j)^2}$

Pixels are characterised by means of calculating the frequency of appearance of the pixels with specific values and spatial relationship influencing the textural allocation in arrangement of the pixels forming a GLCM. Apart from considering only the spectral information for classification of features, GLCM focusses on combination of spatial pattern information that increases the accuracy up to a significant extent. Contrast is the difference moment of GLCM and it measures the spatial frequency of the image. Energy is also known as uniformity or angular second moment. It measures the textural uniformity and detects the disorder in textures. Entropy measures the disorder or complexity of the image. Homogeneity is the inverse difference moment, measures the homogeneous elements of the image and sensitivity to appearance of near diagonal elements. GLCM statistics derived layers with window size of 9x9 are shown in the Fig. 12. With the GLCM statistical layers obtained, a time series band combination layers are plotted to extract the flooded extent. Figure 13 shows the time series band combination of similar GLCM derived statistical layers of different time periods.

Based on the analysis carried out using Sentinel 1 SAR images, the area flooded within the Adyar river basin is obtained and are tabulated in Table 8. Plotting a profile along the flooded extents in the river basin, it is clearly evident from the profiles (pre flood, during floods and post floods) that the backscattering values shows a clear variation along the flooded regions as shown in Fig. 14.

Table 8
 Flooded Extent in Adyar Watershed

Method	Flooded Extent (sq.km)		
	24th November 2015	06th December 2015	18th December 2015
ISODATA Technique	21.76	11.89	09.56
Multi-Temporal Analysis	24.56	12.68	11.65
Thresholding Method	23.37	12.55	10.76
PCA and ICA Analysis	25.65	14.90	12.43
Grey Level Co-Occurrence Matrix	23.15	12.57	11.04

5. Conclusion

Based on the analysis performed, it is clearly evident that the Adyar river and Chembarambakkam reservoir contributed a considerable proportion of water discharge during Chennai floods. Based on the flood report provided by the National Disaster Management Authority, the area of flooded regions in Adyar river basin was reported as 23.5 sq.km and it is evident that the Thresholding (99%) and Grey Level Co-Occurrence Matrix (98.5%) provided better results compared to other methods. The present study demonstrates the accuracy of adopting Sentinel 1 datasets for the extraction of waterbodies. Even though a higher accuracy is achieved, there are certain limitations that has to be taken into consideration

in adopting Sentinel 1 SAR datasets for mapping floods. In flood studies, the acquired Sentinel 1A SAR data is from different time period as of peak flood time because of the revisit time delay. In Sentinel – 1, the revisit day is about 6 days (considering Sentinel 1A and 1B). Frequent visit of SAR sensors enables us for better mapping of flood inundation. Sentinel-1A provides VH and VV polarized data for India rather than HH band for flood mapping. SAR has side looking property, accuracy may vary depending upon the density of build-ups in the study area. Effects such as foreshortening (signal reaches the base of a feature tilted towards the radar), layover (signal return from top of the feature reaches first before the bottom) and shadow (the effect of foreshortening and layover) affects the data. Flooded areas in the built-up (urban) regions are not visible in most of the places, due to the pixel arrangement in Sentinel-1A. It is very unlikely to detect an area with more than 10m space to be flooded in a highly developed and urbanised city.

Declarations

Data availability

The dataset utilized/analyzed during the current study will be available from the corresponding author upon request.

Author contributions

Kiran Yarrakula conceptualized the idea, and provided the necessary resources to carry out this research and supervised Sreechanth Sundaram and Suresh Devaraj throughout this study. Sreechanth Sundaram carried out the review and wrote the manuscript. Suresh Devaraj provided essential technical inputs that helped improve the manuscript.

Declaration of competing interests

The authors declare no competing interests.

Ethical Statement

All ethical practices have been followed in relation to the development, data analysis, writing, and publication of this research article.

Consent to participate

Consent to participate is “Not applicable” for the manuscript.

Consent to publish

None of the data used belongs to any person in any form.

Funding

References

1. Baronti S, Carla R, Sigismondi S, Alparone L (1994) Principal component analysis for change detection on polarimetric multitemporal SAR data. In: Proceedings of IGARSS '94–1994 IEEE International Geoscience and Remote Sensing Symposium. pp 2152–2154 vol.4
2. Beiranvand Pour A, S. Park T-Y, Park Y, et al (2019) Landsat-8, Advanced Spaceborne Thermal Emission and Reflection Radiometer, and WorldView-3 Multispectral Satellite Imagery for Prospecting Copper-Gold Mineralization in the Northeastern Inglefield Mobile Belt (IMB), Northwest Greenland. *Remote Sens* 11:. <https://doi.org/10.3390/rs11202430>
3. Bousquet M (2017) Satellite Communications and Space Telecommunication Frequencies BT - Handbook of Satellite Applications. In: Pelton JN, Madry S, Camacho-Lara S (eds). Springer International Publishing, Cham, pp 325–357
4. Chatenoux B, Richard J-P, Small D, et al (2021) The Swiss data cube, analysis ready data archive using earth observations of Switzerland. *Sci Data* 8:295. <https://doi.org/10.1038/s41597-021-01076-6>
5. Chaudhary MT, Piracha A (2021) Natural Disasters—Origins, Impacts, Management. *Encyclopedia* 1:1101–1131. <https://doi.org/10.3390/encyclopedia1040084>
6. Choi H, Jeong J (2019) Speckle Noise Reduction Technique for SAR Images Using Statistical Characteristics of Speckle Noise and Discrete Wavelet Transform. *Remote Sens* 11:. <https://doi.org/10.3390/rs11101184>
7. Cooper MG, Smith LC (2019) Satellite Remote Sensing of the Greenland Ice Sheet Ablation Zone: A Review. *Remote Sens* 11:. <https://doi.org/10.3390/rs11202405>
8. Dabiri Z, Lang S (2018) Comparison of Independent Component Analysis, Principal Component Analysis, and Minimum Noise Fraction Transformation for Tree Species Classification Using APEX Hyperspectral Imagery. *ISPRS Int J Geo-Information* 7:. <https://doi.org/10.3390/ijgi7120488>
9. Das SK, Gupta RK, Varma HK (2007) Flood and drought management through water resources development in India. *WMO Bull* 56:179–188
10. De Luca G, Silva JMN, Modica G (2021) A workflow based on Sentinel-1 SAR data and open-source algorithms for unsupervised burned area detection in Mediterranean ecosystems. *GIScience Remote Sens* 58:516–541. <https://doi.org/10.1080/15481603.2021.1907896>
11. Devaraj S, Yarrakula K (2020a) Assessment of topographical and atmospheric errors in Sentinel 1 derived DInSAR. *Geocarto Int* 1–17. <https://doi.org/10.1080/10106049.2020.1822926>
12. Devaraj S, Yarrakula K (2020b) Evaluation of Sentinel 1–derived and open-access digital elevation model products in mountainous areas of Western Ghats, India. *Arab J Geosci* 13:1103. <https://doi.org/10.1007/s12517-020-06108-w>

13. Devrani R, Srivastava P, Kumar R, Kasana P (2022) Characterization and assessment of flood inundated areas of lower Brahmaputra River Basin using multitemporal Synthetic Aperture Radar data: A case study from NE India. *Geol J* 57:622–646.
<https://doi.org/https://doi.org/10.1002/gj.4365>
14. Dube K, Nhamo G, Chikodzi D (2021) Flooding trends and their impacts on coastal communities of Western Cape Province, South Africa. *GeoJournal*. <https://doi.org/10.1007/s10708-021-10460-z>
15. Ehrlich D, Melchiorri M, Capitani C (2021) Population trends and urbanisation in mountain ranges of the world. *Land* 10:1–19. <https://doi.org/10.3390/land10030255>
16. Fu W, Ma J, Chen P, Chen F (2020) Remote Sensing Satellites for Digital Earth. In: Guo H, Goodchild MF, Annoni A (eds) *Manual of Digital Earth*. Springer Singapore, Singapore, pp 55–123
17. G Palm B, I Alves D, I Pettersson M, et al (2020) Wavelength-Resolution SAR Ground Scene Prediction Based on Image Stack. *Sensors (Basel)* 20:2008. <https://doi.org/10.3390/s20072008>
18. Harfenmeister K, Spengler D, Weltzien C (2019) Analyzing Temporal and Spatial Characteristics of Crop Parameters Using Sentinel-1 Backscatter Data. *Remote Sens* 11:.
<https://doi.org/10.3390/rs11131569>
19. Huang B, Li Y, Han X, et al (2015) Cloud Removal From Optical Satellite Imagery With SAR Imagery Using Sparse Representation. *IEEE Geosci Remote Sens Lett* 12:1046–1050.
<https://doi.org/10.1109/LGRS.2014.2377476>
20. Ilam Vazhuthi HN, Kumar A (2020) Causes and Impacts of Urban Floods in Indian Cities: A Review. *Int J Emerg Technol* 11:140–147
21. Jiang J, Zhu J, Wang X, et al (2021) Estimating the Leaf Nitrogen Content with a New Feature Extracted from the Ultra-High Spectral and Spatial Resolution Images in Wheat. *Remote Sens* 13:.
<https://doi.org/10.3390/rs13040739>
22. Kookana RS, Drechsel P, Jamwal P, Vanderzalm J (2020) Urbanisation and emerging economies: Issues and potential solutions for water and food security. *Sci Total Environ* 732:139057.
<https://doi.org/https://doi.org/10.1016/j.scitotenv.2020.139057>
23. Ling J, Zhang H, Lin Y (2021) Improving urban land cover classification in cloud-prone areas with polarimetric sar images. *Remote Sens* 13:.
<https://doi.org/10.3390/rs13224708>
24. Manavalan R (2018) Review of synthetic aperture radar frequency, polarization, and incidence angle data for mapping the inundated regions. *J Appl Remote Sens* 12:1–15.
<https://doi.org/10.1117/1.JRS.12.021501>
25. Martinis S, Rieke C (2015) Backscatter Analysis Using Multi-Temporal and Multi-Frequency SAR Data in the Context of Flood Mapping at River Saale, Germany. *Remote Sens* 7:7732–7752.
<https://doi.org/10.3390/rs70607732>
26. Misra T (2017) Indian Remote Sensing Sensor System: Current and Future Perspective. *Proc Natl Acad Sci India Sect A Phys Sci* 87:473–486. <https://doi.org/10.1007/s40010-017-0429-7>
27. Nagai H, Abe T, Ohki M (2021) SAR-Based Flood Monitoring for Flatland with Frequently Fluctuating Water Surfaces: Proposal for the Normalized Backscatter Amplitude Difference Index (NoBADI).

- Remote Sens 13:. <https://doi.org/10.3390/rs13204136>
28. Nagler T, Rott H, Hetzenecker M, et al (2015) The Sentinel-1 Mission: New Opportunities for Ice Sheet Observations. *Remote Sens* 7:9371–9389. <https://doi.org/10.3390/rs70709371>
29. Ouled Sghaier M, Hammami I, Foucher S, Lepage R (2018) Flood Extent Mapping from Time-Series SAR Images Based on Texture Analysis and Data Fusion. *Remote Sens* 10:. <https://doi.org/10.3390/rs10020237>
30. Pepe A, Calò F (2017) A review of interferometric synthetic aperture RADAR (InSAR) multi-track approaches for the retrieval of Earth's Surface displacements. *Appl Sci* 7:. <https://doi.org/10.3390/app7121264>
31. Prieto-Amparan JA, Villarreal-Guerrero F, Martinez-Salvador M, et al (2018) Atmospheric and Radiometric Correction Algorithms for the Multitemporal Assessment of Grasslands Productivity. *Remote Sens* 10:. <https://doi.org/10.3390/rs10020219>
32. Rad AM, Kreitler J, Sadegh M (2021) Augmented Normalized Difference Water Index for improved surface water monitoring. *Environ Model Softw* 140:105030. <https://doi.org/https://doi.org/10.1016/j.envsoft.2021.105030>
33. Rasti B, Scheunders P, Ghamisi P, et al (2018) Noise Reduction in Hyperspectral Imagery: Overview and Application. *Remote Sens* 10:. <https://doi.org/10.3390/rs10030482>
34. Reddy KR, Devaraj S, Biradar S, et al (2019) Spatial distribution of land use/ land cover analysis in Hanamkonda taluk, Telangana - A case study. *Indian J Geo-Marine Sci* 48:1761–1768
35. Ruggeri S, Henao-Céspedes V, Garcés-Gómez YA, Parra Uzcátegui A (2021) Optimized unsupervised CORINE Land Cover mapping using linear spectral mixture analysis and object-based image analysis. *Egypt J Remote Sens Sp Sci* 24:1061–1069. <https://doi.org/https://doi.org/10.1016/j.ejrs.2021.10.009>
36. Song X-P, Huang W, Hansen MC, Potapov P (2021) An evaluation of Landsat, Sentinel-2, Sentinel-1 and MODIS data for crop type mapping. *Sci Remote Sens* 3:100018. <https://doi.org/https://doi.org/10.1016/j.srs.2021.100018>
37. Soudani K, Delpierre N, Berveiller D, et al (2021) Potential of C-band Synthetic Aperture Radar Sentinel-1 time-series for the monitoring of phenological cycles in a deciduous forest. *Int J Appl Earth Obs Geoinf* 104:102505. <https://doi.org/https://doi.org/10.1016/j.jag.2021.102505>
38. Sundaram S, Devaraj S, Yarrakula K (2021) Modeling, mapping and analysis of urban floods in India –a review on geospatial methodologies. *Environ Sci Pollut Res* 28:67940–67956. <https://doi.org/10.1007/s11356-021-16747-5>
39. Surampudi S, Yarrakula K (2020) Mapping and assessing spatial extent of floods from multitemporal synthetic aperture radar images: a case study on Brahmaputra River in Assam State, India. *Environ Sci Pollut Res* 27:1521–1532. <https://doi.org/10.1007/s11356-019-06849-6>
40. Suresh D, Collins Johnny J, Jayaprasad BK, et al (2018) Morphometric analysis for identification of groundwater recharge zones: A case study of Neyyar river basin. *Indian J Geo-Marine Sci* 47:1969–1979

41. Suresh D, Yarrakula K (2018) Subsidence monitoring techniques in coal mining: Indian scenario. *Indian J Geo-Marine Sci* 47:1918–1933
42. Talukdar S, Singha P, Mahato S, et al (2020) Land-Use Land-Cover Classification by Machine Learning Classifiers for Satellite Observations—A Review. *Remote Sens* 12:. <https://doi.org/10.3390/rs12071135>
43. Tatem AJ, Goetz SJ, Hay SI (2008) Fifty Years of Earth Observation Satellites: Views from above have lead to countless advances on the ground in both scientific knowledge and daily life. *Am Sci* 96:390–398. <https://doi.org/10.1511/2008.74.390>
44. Ustin SL, Middleton EM (2021) Current and near-term advances in Earth observation for ecological applications. *Ecol Process* 10:1. <https://doi.org/10.1186/s13717-020-00255-4>
45. Vargas JF, Ferrer MA, Travieso CM, Alonso JB (2011) Off-line signature verification based on grey level information using texture features. *Pattern Recognit* 44:375–385. <https://doi.org/10.1016/j.patcog.2010.07.028>
46. Vickers H, Malnes E, Høgda K-A (2019) Long-Term Water Surface Area Monitoring and Derived Water Level Using Synthetic Aperture Radar (SAR) at Altevåtn, a Medium-Sized Arctic Lake. *Remote Sens* 11:. <https://doi.org/10.3390/rs11232780>
47. Vivekananda GN, Swathi R, Sujith A (2021) Multi-temporal image analysis for LULC classification and change detection. *Eur J Remote Sens* 54:189–199. <https://doi.org/10.1080/22797254.2020.1771215>
48. Wang SW, Munkhnasan L, Lee W-K (2021) Land use and land cover change detection and prediction in Bhutan's high altitude city of Thimphu, using cellular automata and Markov chain. *Environ Challenges* 2:100017. <https://doi.org/https://doi.org/10.1016/j.envc.2020.100017>
49. Xue J, Su B (2017) Significant Remote Sensing Vegetation Indices: A Review of Developments and Applications. *J Sensors* 1353691:17. <https://doi.org/10.1155/2017/1353691>
50. You Y, Cao J, Zhou W (2020) A survey of change detection methods based on remote sensing images for multi-source and multi-objective scenarios. *Remote Sens* 12:. <https://doi.org/10.3390/RS12152460>
51. Zainal Z, Ramli R, Mustafa MM (2013) Grey-Level Cooccurrence Matrix Performance Evaluation for Heading Angle Estimation of Moveable Vision System in Static Environment. *J Sensors* 2013:624670. <https://doi.org/10.1155/2013/624670>
52. Zhang M, Chen F, Liang D, et al (2020) Use of sentinel-1 grd sar images to delineate flood extent in Pakistan. *Sustain* 12:1–19. <https://doi.org/10.3390/su12145784>

Figures

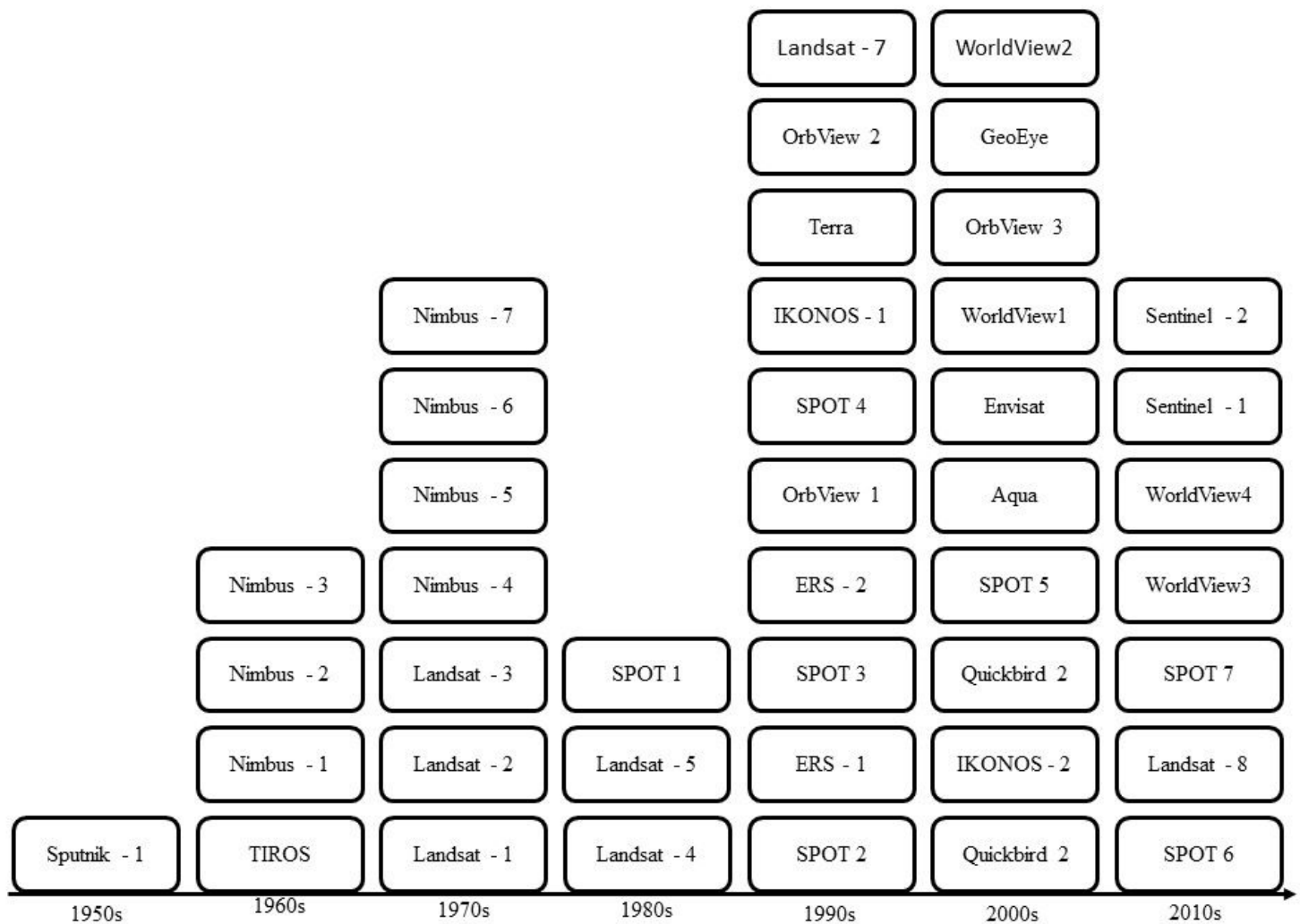


Figure 1

Evolution of space age with few major space missions since 1950s.

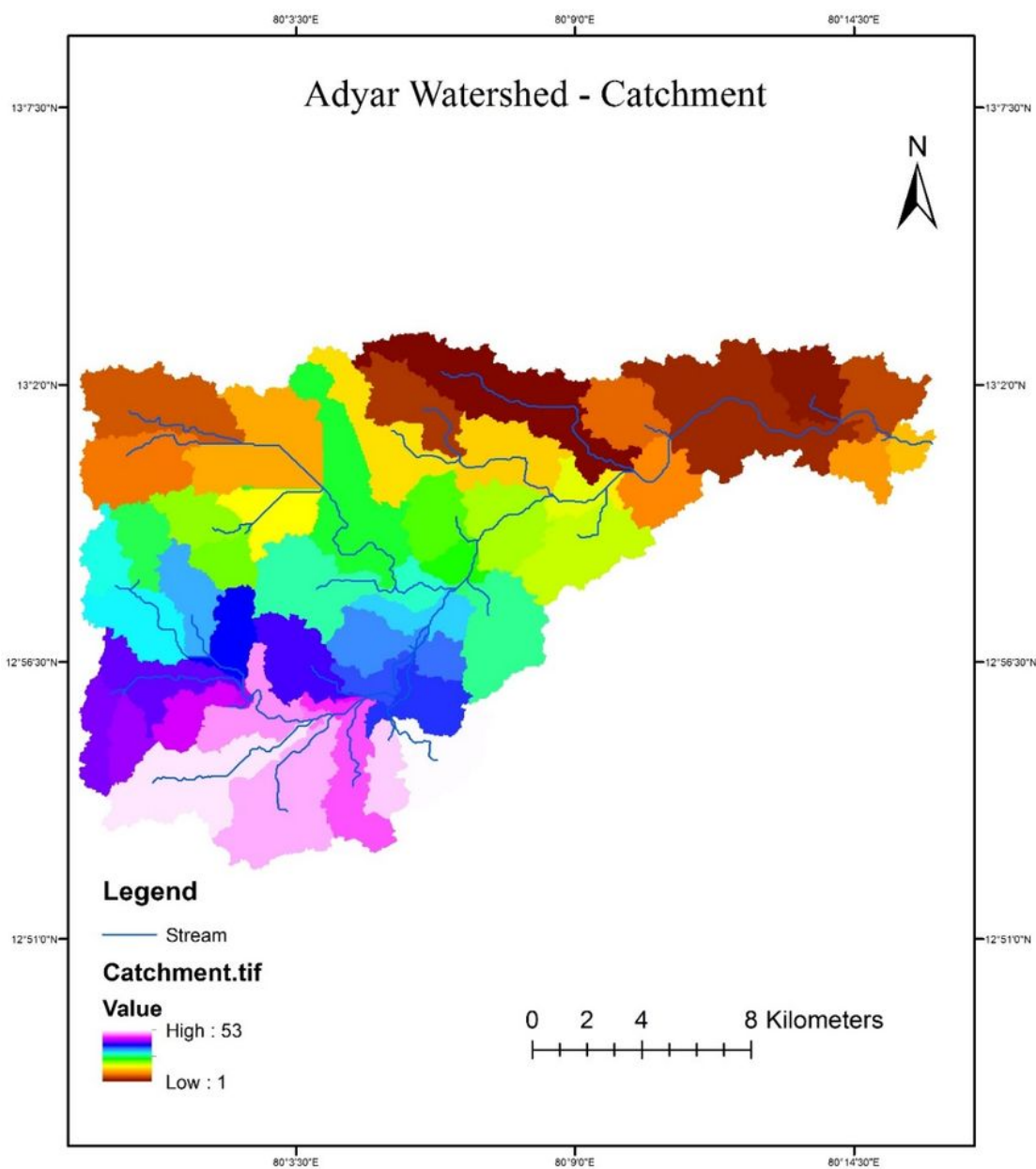


Figure 2

Adyar River Catchment Map (Sub-Watersheds)

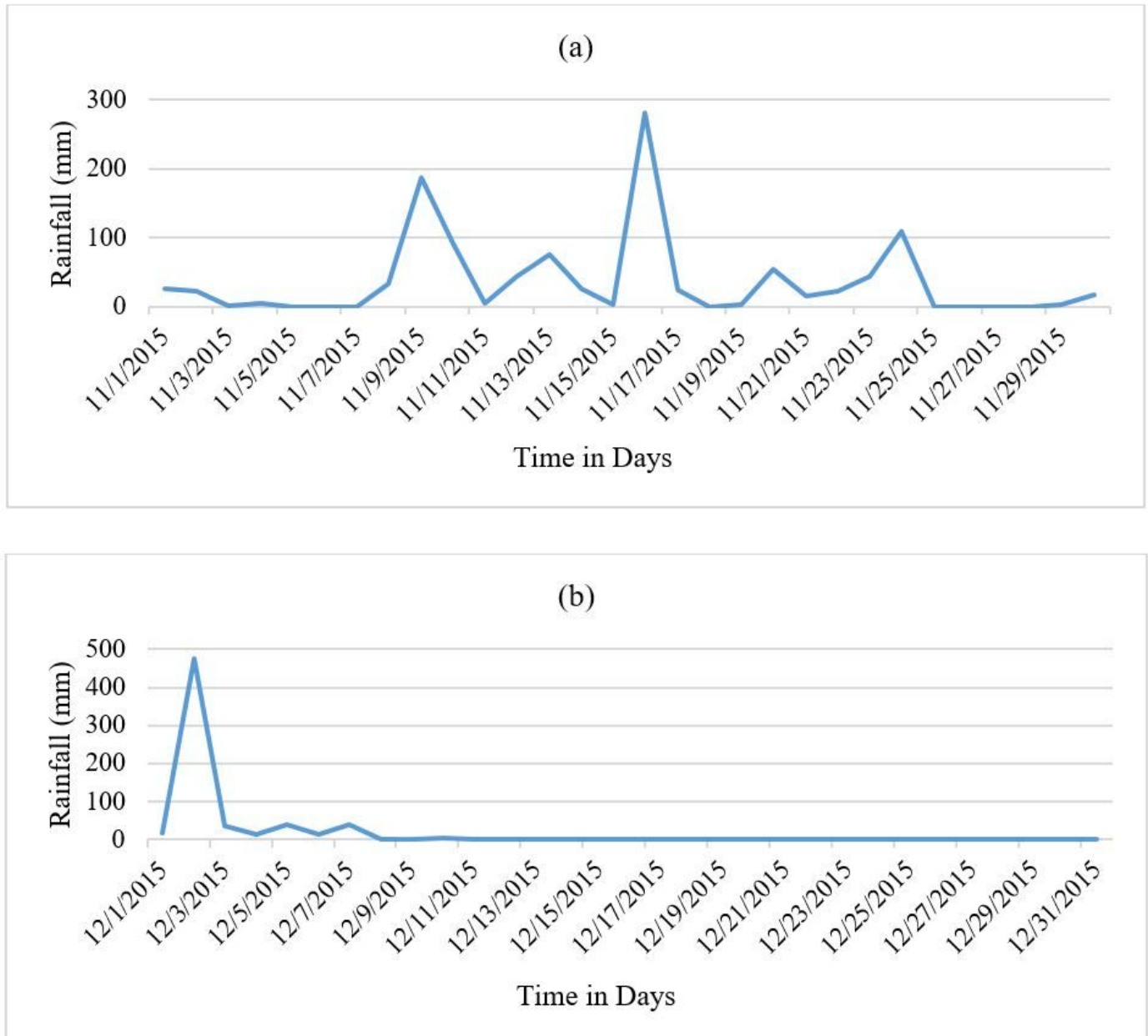


Figure 3

Observed Rainfall in Chembarambakkam Reservoir – November 2015 (a) November month (b) December month

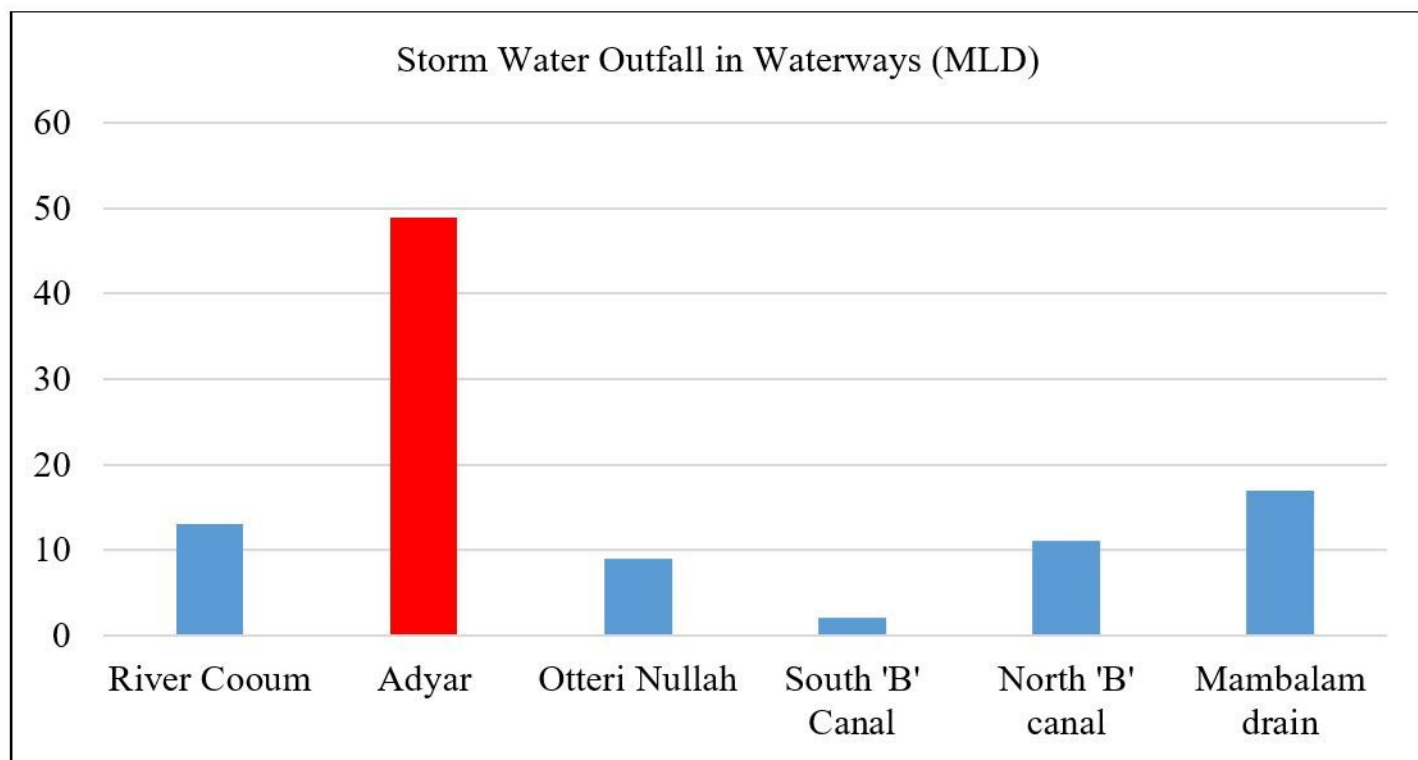


Figure 4

Storm Water Outfall in Chennai City

(Source: Chennai Metropolitan Development Authority, CMDA)

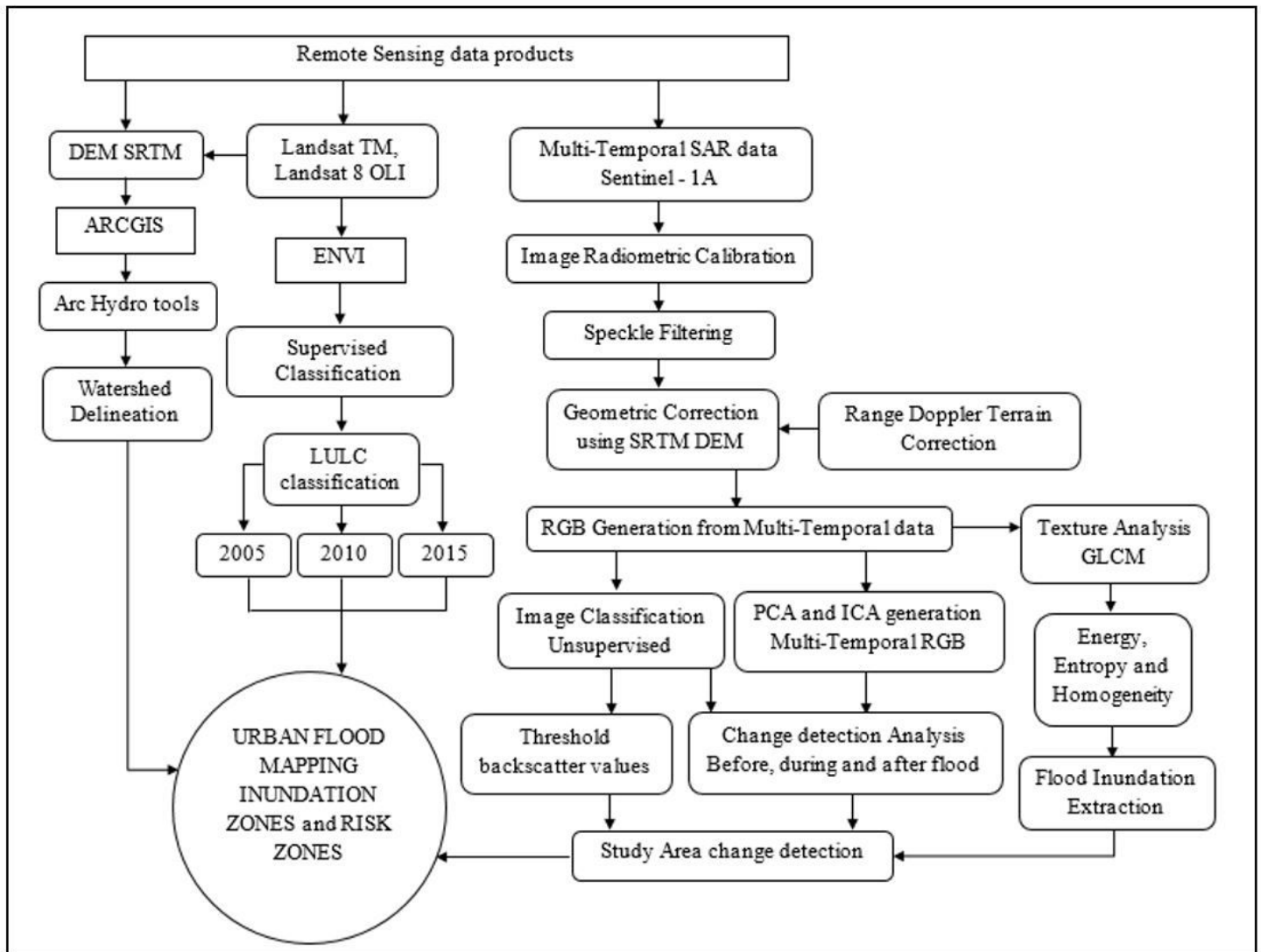
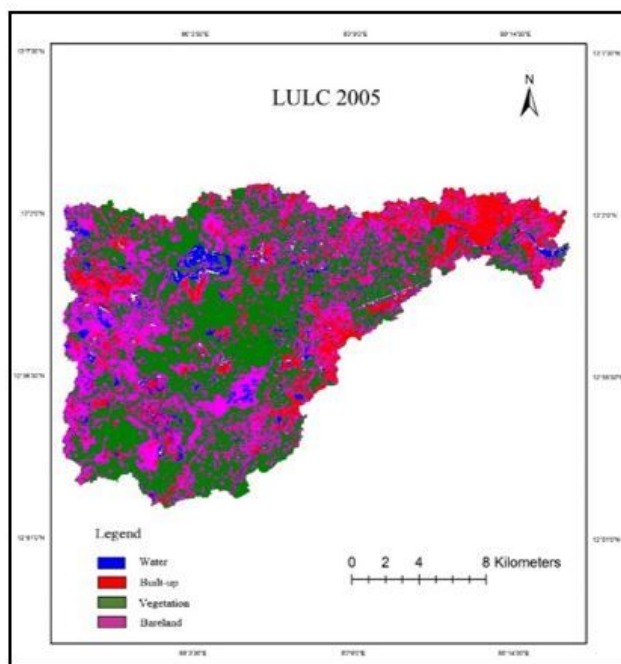
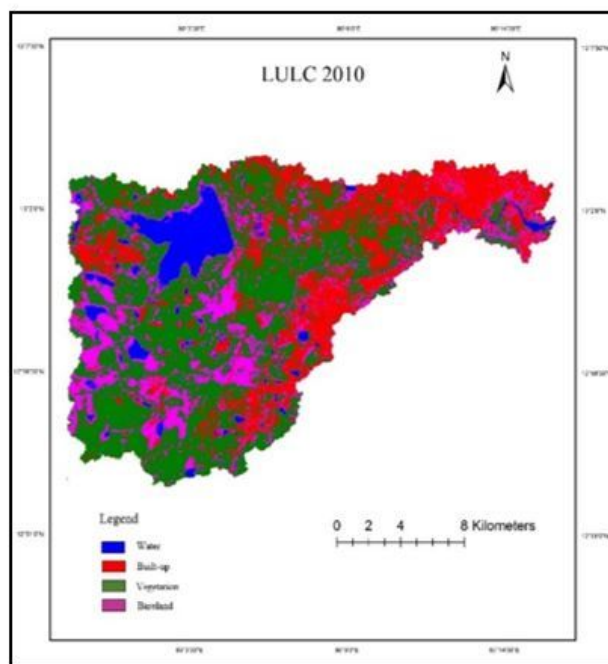


Figure 5

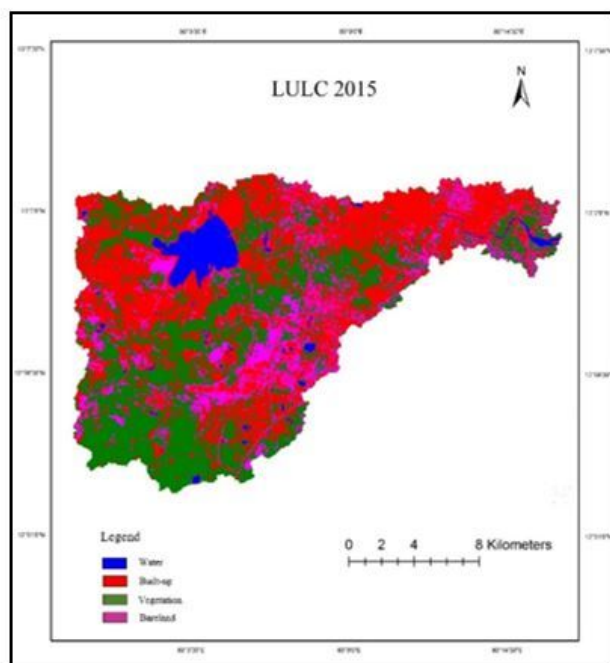
Flow Chart of Methodology Used for Extracting Flooded Regions



(a)



(b)



(c)

Figure 6

Land Use Land Cover Map – Adyar Watershed (a) 2005 (b) 2010 (c) 2015

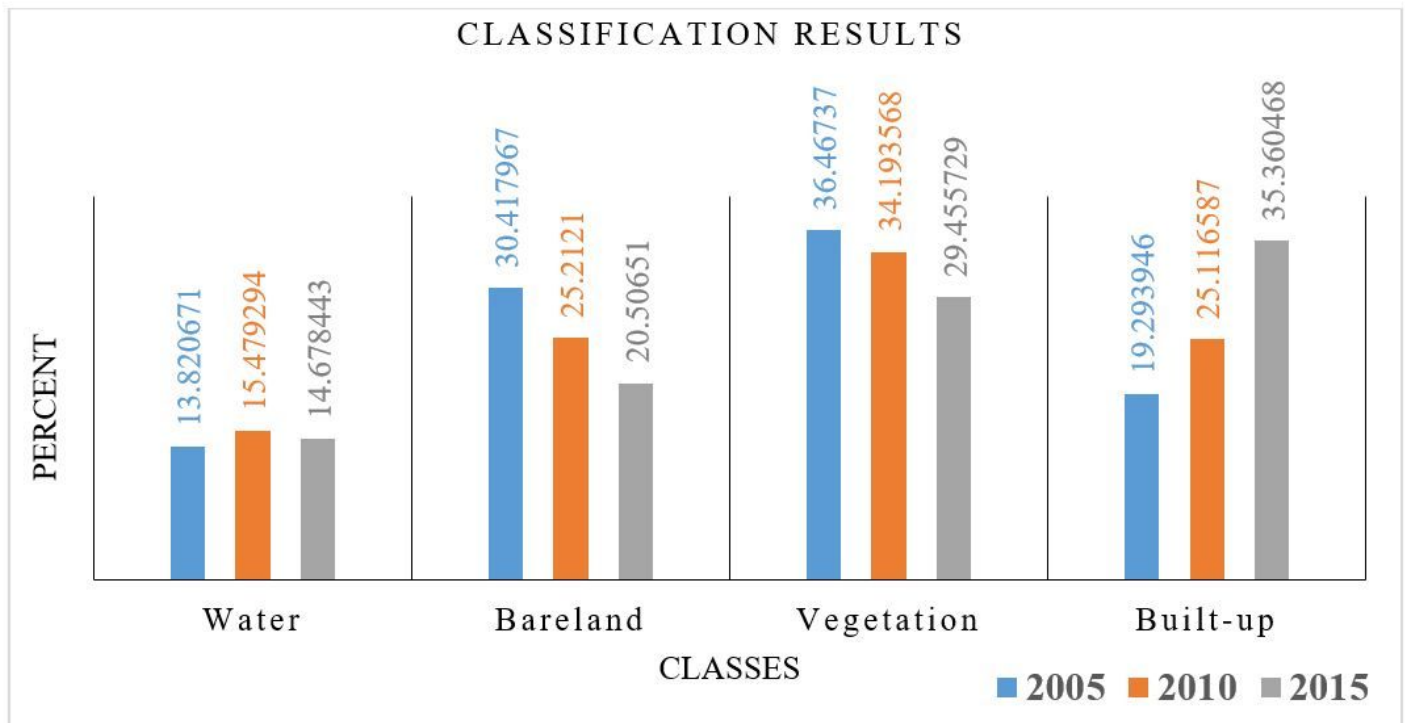
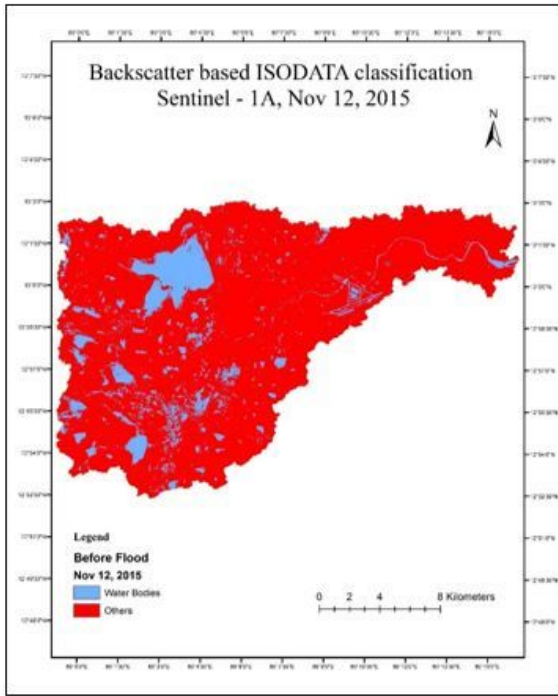
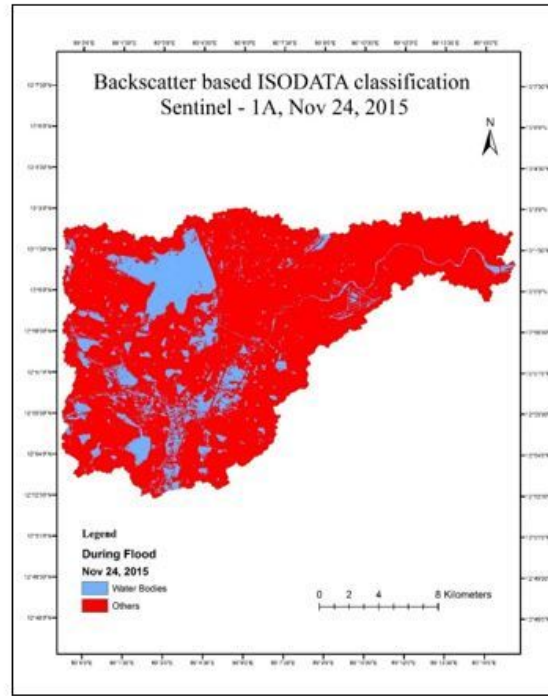


Figure 7

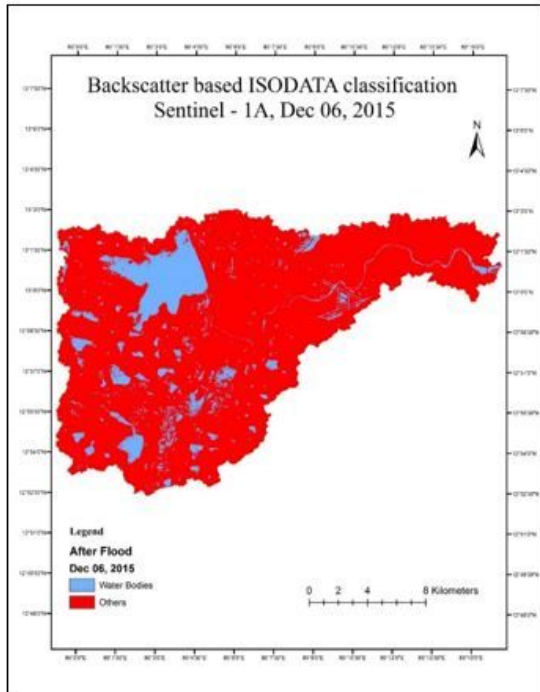
Change Detection Statistics of 2005, 2010 And 2015 For Adyar Watershed



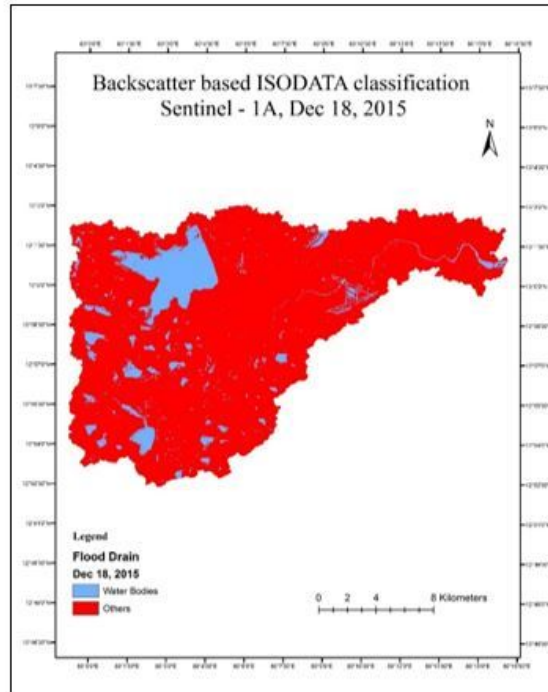
(a) 12th November 2015



(b) 24th November 2015



(c) 06th December 2015



(d) 18th December 2015

Figure 8

Unsupervised Classification of Sentinel 1A SAR Data (a) 12th November 2015 (b) 24th November 2015 (c) 06th December 2015 (d) 18th December 2015

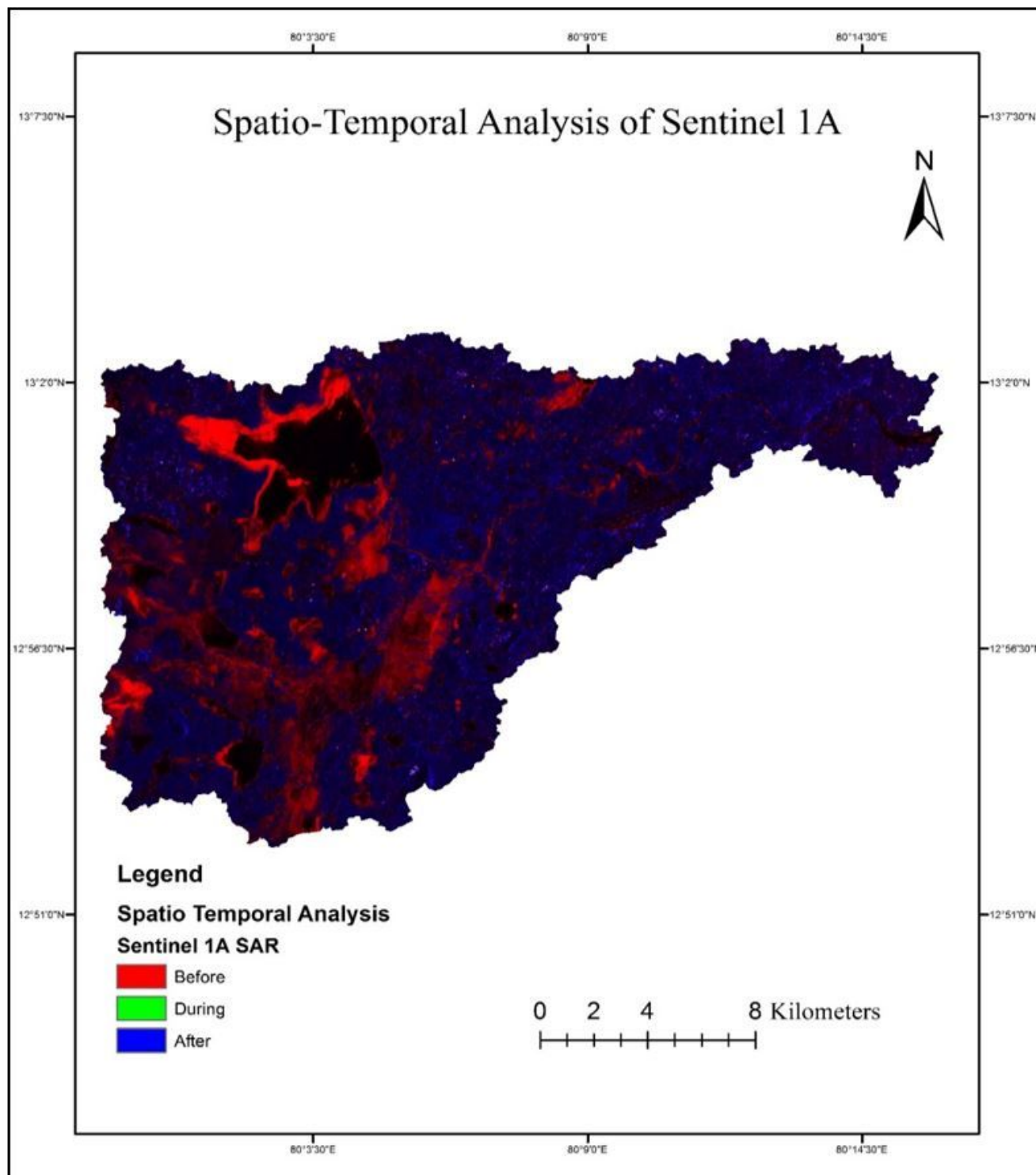


Figure 9

Sentinel 1A Spatio-Temporal Analysis

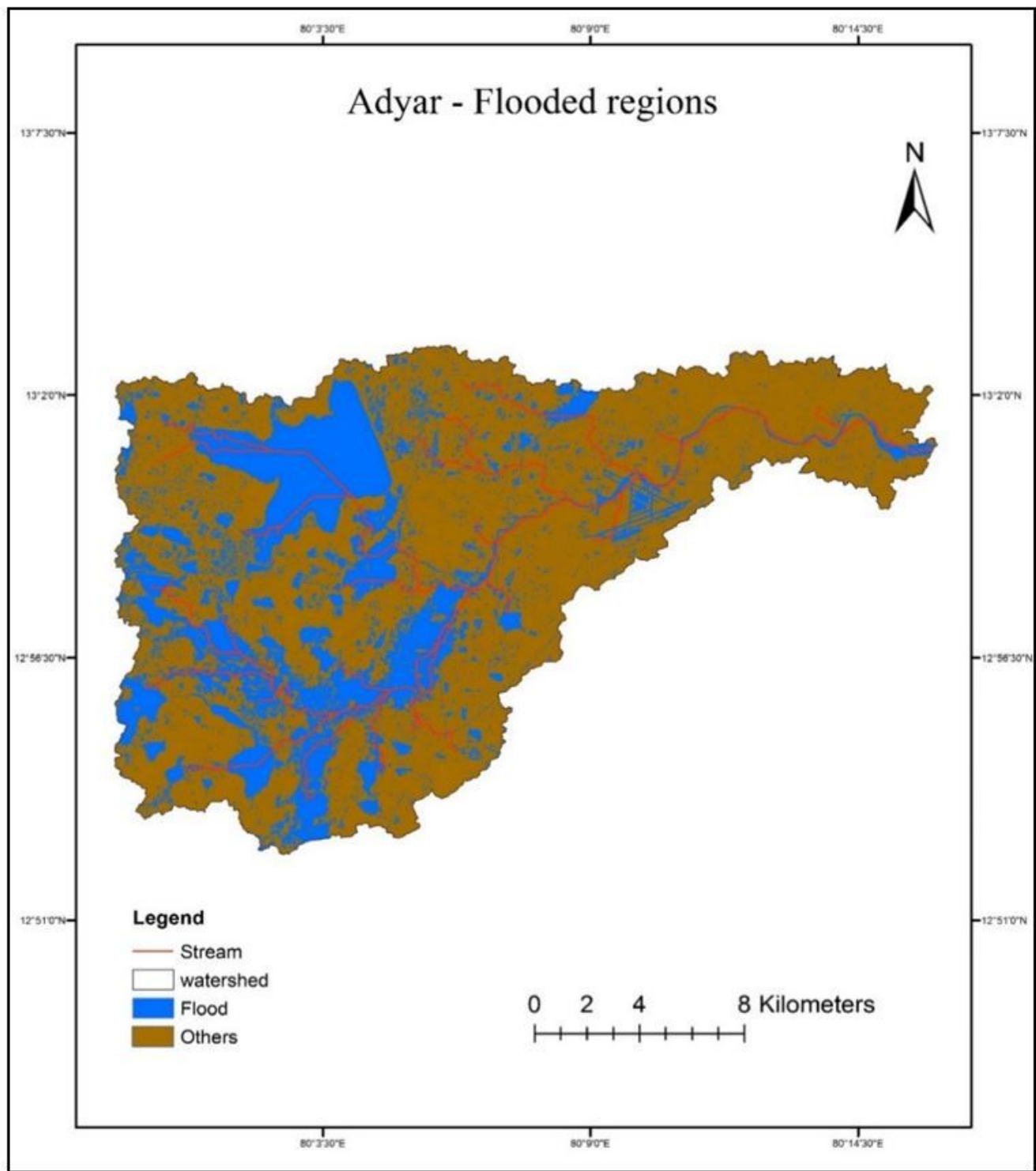


Figure 10

Flooded Regions Extracted from Backscatter Values using Thresholding Method

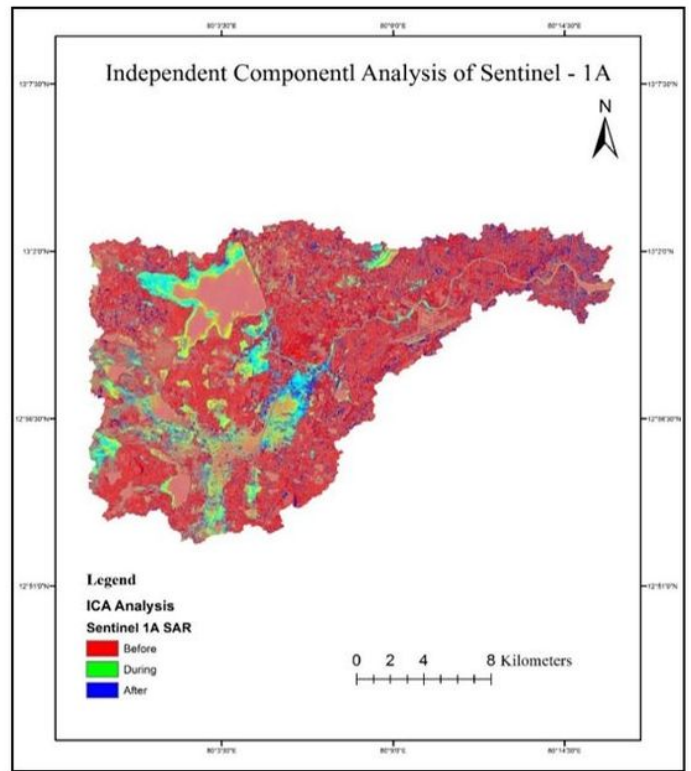
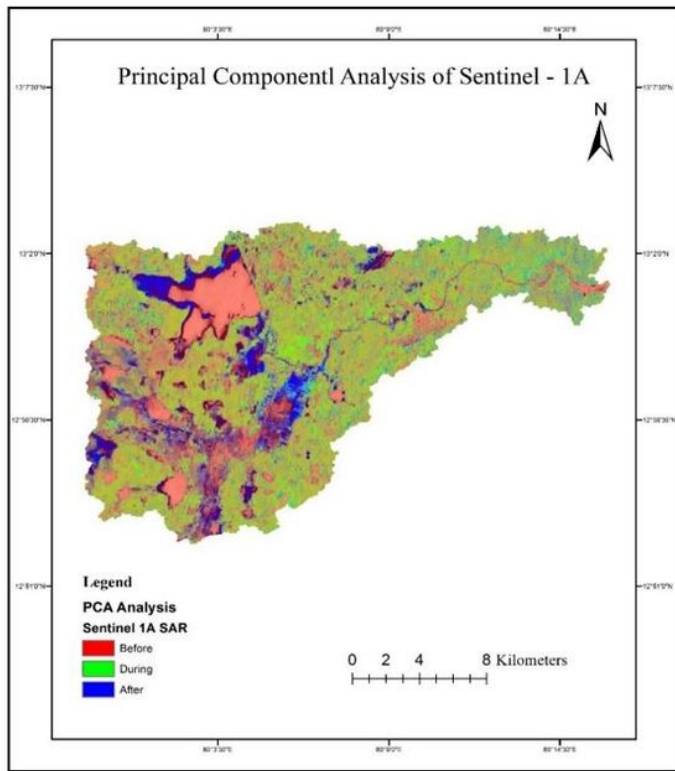
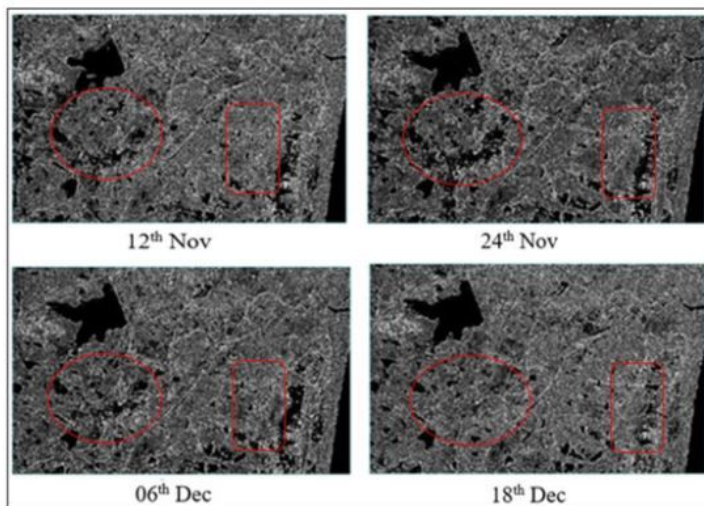


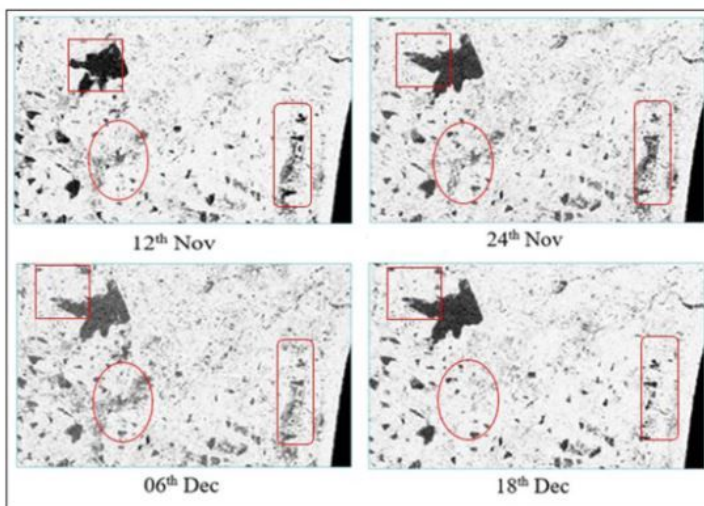
Figure 11

(a) Principal Component Analysis on Multi-Temporal Sentinel -1A SAR

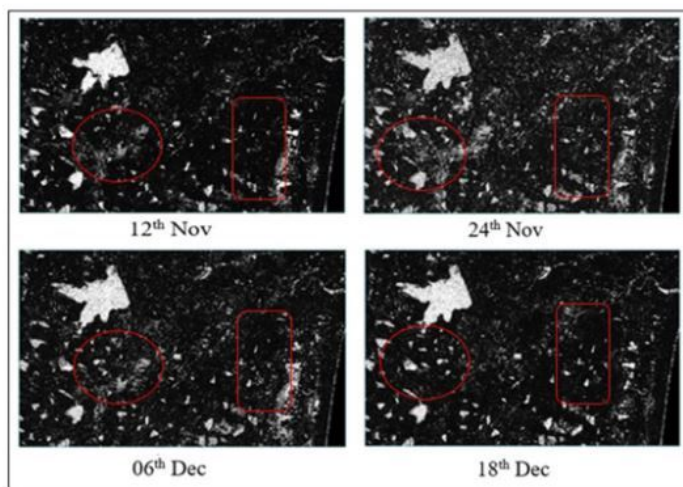
(b) Independent Component Analysis on Multi-Temporal Sentinel -1A SAR



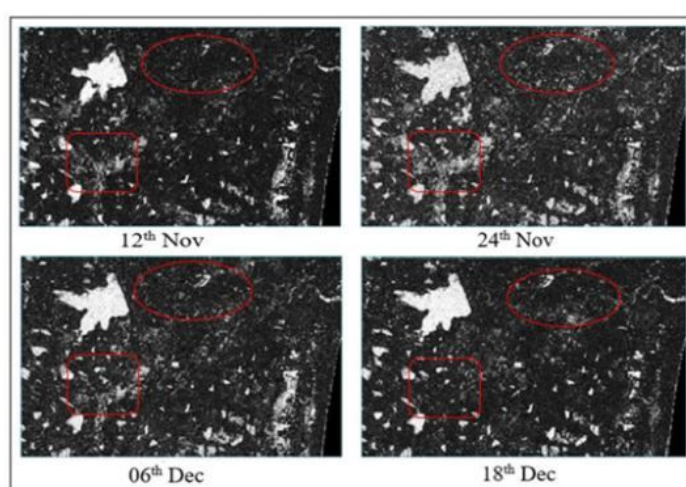
(a) Contrast Layer



(c) Entropy Layer



(b) Energy Layer



(d) Homogeneity Layer

Figure 12

GLCM statistics Generated From Sentinel – 1A SAR Data

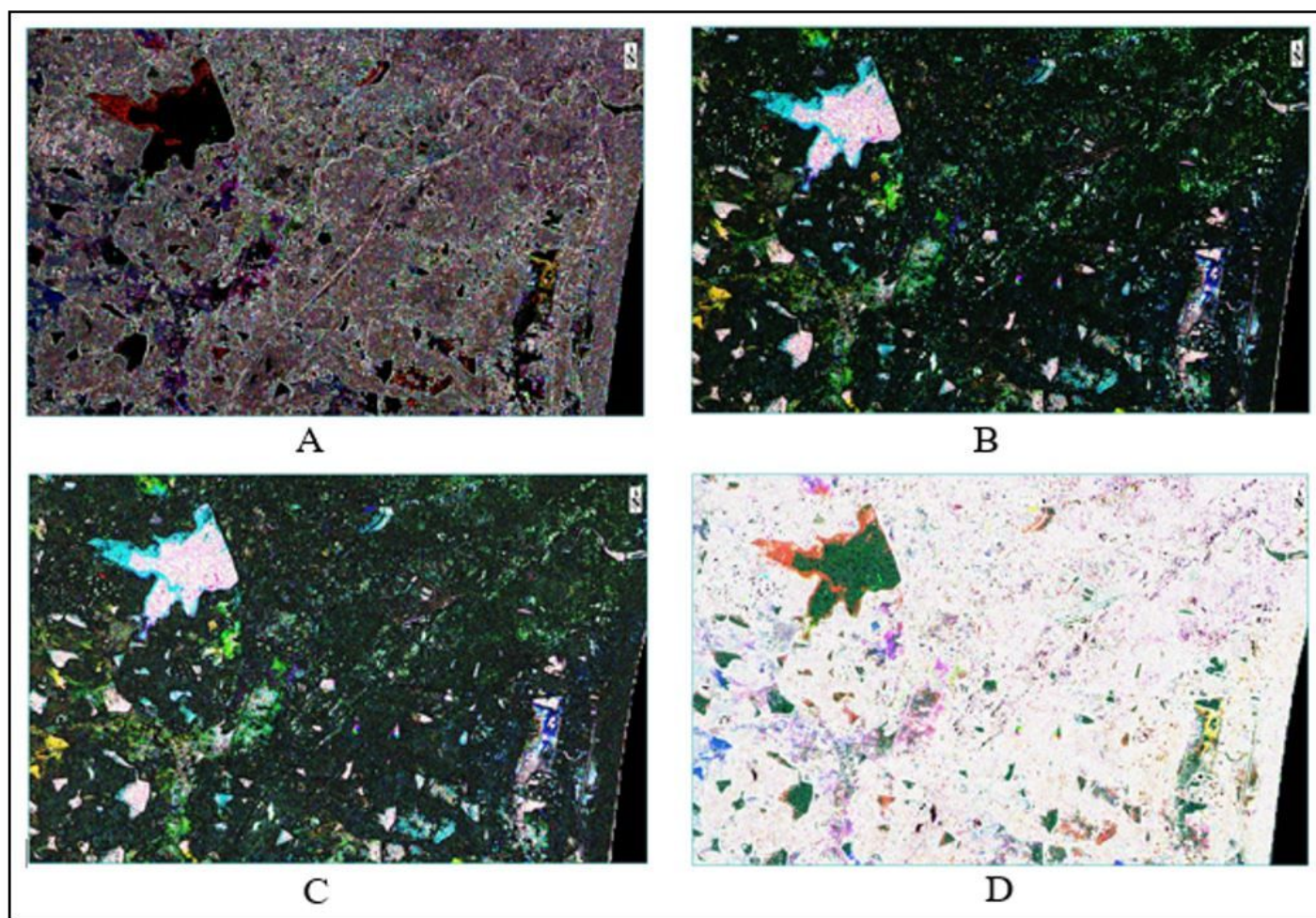
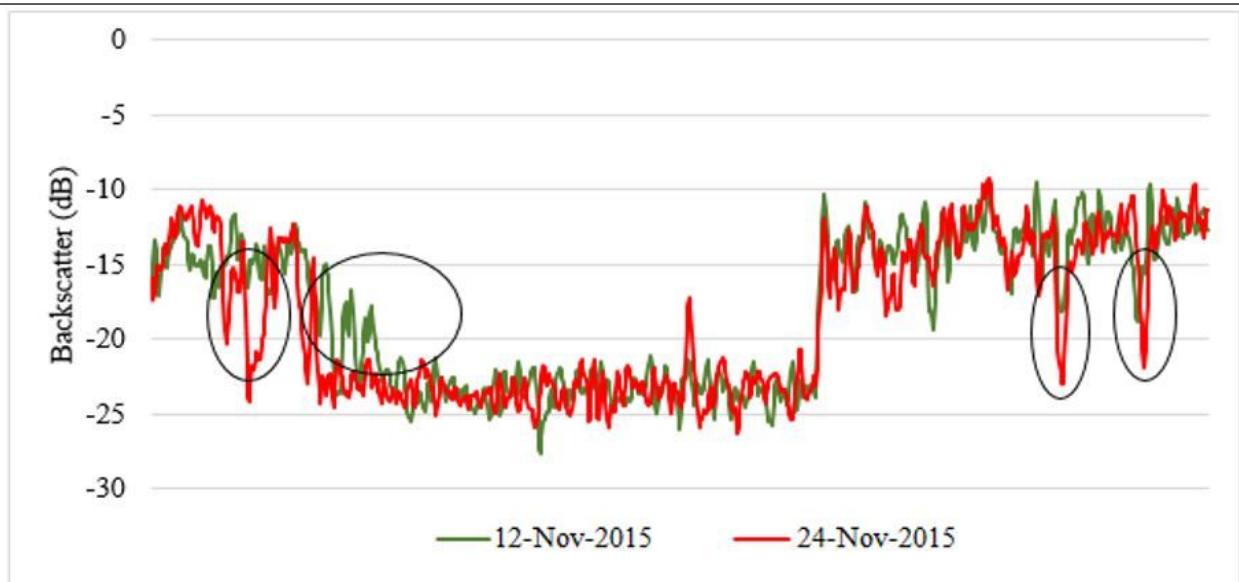
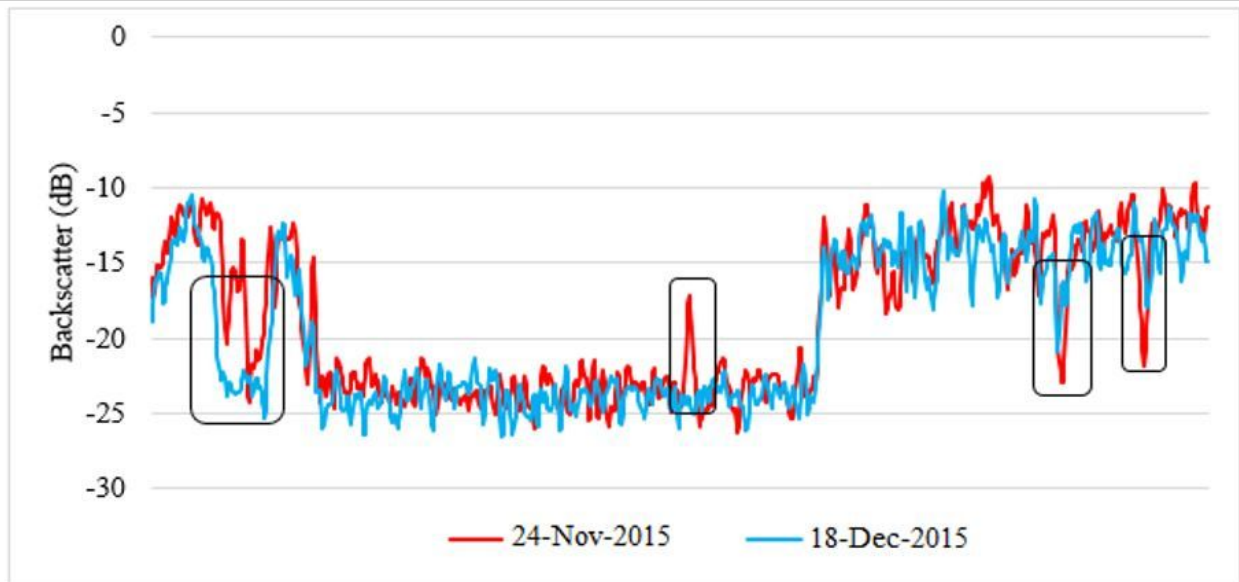


Figure 13

Time-Series (Multi-Date) Layer Generated From Sentinel – 1A Using GLCM Statistics A) Contrast B) Energy C) Homogeneity D) Entropy



(a) Pre Flood vs During Flood



(b) During Flood vs Post Flood

Figure 14

Backscatter Profile